Research Square

Preprints are preliminary reports that have not undergone peer review.
They should not be considered conclusive, used to inform clinical practice,
or referenced by the media as validated information.

Unfolding the Hidden Message of Anode-Free Lithium Metal Battery

Chen-Jui Huang
National Taiwan University of Science and Technology https://orcid.org/0000-0001-8338-1424
Balamurugan Thirumalraj
National Taiwan University of Science and Technology https://orcid.org/0000-0001-9369-1901
Hsien-Chu Tao
National Taiwan University of Science and Technology
Kassie Nigus Shitaw
National Taiwan University of Science and Technology
Tesfaye Teka Hagos
National Taiwan University of Science and Technology
Tamene Tadesse Beyene
National Taiwan University of Science and Technology
Li-Ming Kuo
National Taiwan University of Science and Technology
Chun-Chieh Wang
National Synchrotron Radiation Research Center
She-huang Wu
National Taiwan University of Science and Technology
Wei-Nien Su
National Taiwan University of Science and Technology https://orcid.org/0000-0003-1494-2675
Bing Joe Hwang (bjh@mail.ntust.edu.tw)
National Taiwan University of Science and Technology https://orcid.org/0000-0002-3873-2149

Article

Keywords: Lithium metal batteries, anode-free lithium metal batteries, energy density

Posted Date: July 29th, 2020

DOI: https://doi.org/10.21203/rs.3.rs-45279/v1

License: This work is licensed under a Creative Commons Attribution 4.0 International License.
Read Full License

Version of Record: A version of this preprint was published at Nature Communications on March 4th, 2021. See the published version at https://doi.org/10.1038/s41467-021-21683-6.

Unfolding the Hidden Message of Anode-Free Lithium Metal Battery

Chen-Jui Huang[1], Balamurugan Thirumalraj[1], Hsien-Chu Tao[1], Kassie Nigus Shitaw[1], Hogiartha Sutiono[1], Tesfaye Teka Hagos[2], Tamene Tadesse Beyene[1], Li-Ming Kuo[1], Chun-Chieh Wang[3], She-Huang Wu[2], Wei-Nien Su[2], Bing Joe Hwang[1,3,4*]

[1]Department of Chemical Engineering, National Taiwan University of Science and Technology, Taipei, Taiwan

[2]Graduate Institute of Applied Science and Technology, National Taiwan University of Science and Technology, Taipei, Taiwan

[3]National Synchrotron Radiation Research Center (NSRRC), Hsinchu, Taiwan

[4]Sustainable Energy Development Center, National Taiwan University of Science and Technology, Taipei, Taiwan

e-mail:bjh@mail.ntust.edu.tw

Abstract

Lithium metal batteries (LMBs) have been revisited and gained great attention due to significantly mitigated formation of Li dendrite in the past decade. Recently, anode-free lithium metal batteries (AFLMBs) are proposed and have been studied intensively to potentially outperform LMBs due to higher energy density and reduced safety hazards since the absence of Li metal during the fabrication process of the cell. In general, researchers compare capacity retention, reversible capacity, or rate capability of the cells to study the electrochemical performance of batteries. However, evaluating the behavior of batteries from limited aspects would easily overlook other information hidden deep inside the meretricious results or even lead to misguided data interpretation. In this work, an integrated protocol combining different types of cell configuration is proposed and validated for the first time to unravel the concealed messages in LMBs and AFLMBs. Irreversible coulombic efficiency (irr-CE) from various contributions including reductive electrolyte decomposition, dead Li formation, 1st intrinsic irreversible capacity of a cathode, and the subsequent irreversible reactions at cathode containing oxidative electrolyte decomposition and cathode degradation upon cycling are successfully determined separately by the integrated protocol for the first time. The decrypted information obtained from the proposed protocol provides an insightful understanding of behaviors of LMBs and AFLMBs, which promotes their development for practical applications.

Lithium metal, with an ultrahigh theoretical specific capacity (3,860 mAh g^{-1}) and extremely low redox potential (-3.040 V vs. standard hydrogen electrode), has already been extensively investigated over the four decades[1, 2]. However, lithium metal batteries (LMB) still suffer from several barriers and yet to be commercialized. More specifically, the safety issues induced by Li dendrite growth and internal short-circuit (ISC)[3], poor efficiency attributed to the formation of high surface area lithium (HSAL, dendrite) and dead Li[4, 5], and severe electrolyte decomposition at the negative electrode leading to electrolyte dry-up and the formation of thick solid electrolyte interphase (SEI) that increases the internal resistance and consumes the electrolytes[6, 7, 8, 9, 10].

To overcome the aforementioned challenges, one has to systematically study Li metal stability/protection[11], SEI formation mechanism[12, 13], and suppression of Li dendrite growth in LMB[14, 15, 16]. Many works have also been done by using different electrolyte formulas, surface modified Li, and artificial coating layers to study their effect on increasing the electrochemical performance of LMB. Meanwhile, several key factors would still affect the cycling performance of LMB and are crucial in achieving high specific energy of 500 Wh kg^{-1} demanded by electric vehicle energy-storage market such as electrolyte amount[17], temperature[18], pressure[19], amount of Li or cahode[20, 21], and current density applied[9], etc. Recently, Anode-free lithium metal batteries (AFLMBs) are considered as phenomenal energy storage systems due to higher energy density than that of LMB which with excess Li in the system, and greatly reduced safety risks since no Li metal is used during cell manufacturing, which remarkably increases the simplicity of cell fabrication and reduces the cost of cell assembly, too[22, 23, 24, 25, 26, 27].

However, in most of the published works, the electrochemical performance of LMBs/AFLMBs is often discussed by comparing capacity retention, reversible capacity, or rate capability, which easily overlooks or even misunderstands the information that is concealed by the meretricious results when adopting only one or two points of view. To systematically evaluate the electrochemical performance of both LMBs and AFLMBs, and unfold all the messages hidden within the battery, one has to comprehensively examine the information from all the possible perspectives. More importantly, integrating all the unraveled phenomena and messages to have a better overall evaluation of the battery systems is essential.

In this work, we systematically study four different types of cell configuration, including Li//Li symmetric cells[28], Li//Cu cells, cathode/Li cells, and cathode/Cu anode-free cells, as an integrated protocol to unfold the intrinsic reasons and contributions of individual irreversible coulombic efficiency (irr-CE) in LMBs or AFLMBs. Meanwhile, we also observed dendritic Li induced internal short-circuit and visualize the formation of dead Li in a Li//Cu cell using *in-situ* optical microscopy (OM) and transmission X-ray microscopy (TXM), and proposed the mechanism of Li nucleation and deposition/dissolution on Cu.

Results

***In-situ* OM observation of Li deposition/dissolution.** Li deposition/dissolution upon cycling with the subsequent dendrite growth and formation of dead Li are observed by *in-situ* OM in Fig. 1a. In the beginning, both Cu and Li surfaces are very smooth. In the first 10 seconds of plating, there was a clear potential drop observed from the curve, which was due to the overpotential induced by the initial nucleation of Li on Cu foil and SEI fracture. After the nucleation sites were formed, the polarization was found reduced. The plated Li was homogeneous and dense during the first 100 seconds, however, granular Li started to grow on different spots of Cu foil due to the inhomogeneous plating of Li. After the initial granular Li emerged, which served as a new nucleus, high surface area lithium (HSAL) vigorously grew on top of the granule rather than the compact and uniform Li beside it on Cu foil. Additionally, non-uniform dissolution of Li and formation of a rough surface at the Li electrode were also observed during the first 300 seconds, induced from the locally heterogeneous current distribution, which also accelerated the formation of dendritic Li on the Cu electrode.

As the plating process continued, the HSAL eventually contacted the Li electrode and short-circuits occurred after 300 seconds of Li plating. Then, the cell voltage was found suddenly lifted to -0.022 V vs. $Li//Li^+$ but not zero, indicating there is an SEI resistance between two contacted electrodes. Although the potentiostat was still applying negative current, no extra Li was plated on the working electrode during the short-circuit. When the cell was switched to a stripping mode at 650 seconds, the slightly positive cell voltage of 0.022V vs. $Li//Li^+$ was also observed in the stripping process due to the SEI resistance between both contacted electrodes as in the deposition process. Besides, the morphology of the dendrite kept unchanged without Li deposition/dissolution during the short-circuit.

After 740 seconds at the stripping process, the short-circuited HSAL between two electrodes suddenly disconnected and started to dissolve. However, dead Li was discovered after 40 seconds of stripping as the HSAL stopped dissolving due to the higher charge resistance, leaving a large amount of dead Li on the Cu surface at the end of the stripping process. This results in poor CE observed from the cycling performance of the cell.

Li nucleation and deposition/dissolution mechanism. Based on the OM (see Fig. 1a) and TXM (see Fig. S1) observation of Li plating/stripping, the electrochemical phenomena of Li plating/stripping on Cu is investigated and the corresponding proposed mechanism is shown in Fig. 1b. During the very beginning of Li deposition on Cu foil, an initial energy barrier needs to be overcome by first forming nucleation sites on the clean Cu surface, which causes the initial higher overpotential seen from the curve. Then, Li underneath the thick SEI layer on Li foil starts to dissolve and deposit onto the nucleation sites on the Cu surface, accompanied by the decrease of overpotential. Next, in the Li stripping process from the Cu surface, the overpotential is induced from the resistance of SEI layer protruding and fresh Li growth on the Li surface. At the end of the Li stripping process from the Cu surface, the cell voltage suddenly lifted due to the full consumption of active Li, leaving some amount of dead Li at the Cu side. From our previous results obtained from *in-situ* Transmission X-ray Microscopy (TXM)[4], we observed that the formation of dead Li is normally from the outer part of deposited Li which disconnects with the active Li at the electrode surface, similar to the observation in this work, and the stacking of dead Li is also observed after several plating/stripping processes. At the same time on the other side, dendrites start to evolve on the roughened Li surface due to non-uniform current distribution from the previous dissolution process. In the following cycles, the deposition/dissolution of Li is similar to the first cycle in general, including SEI fracture, fresh Li nucleation, dendrite growth, and dead Li formation at both sides. More detail regarding the SEI fracture mechanism is discussed in our recent work[29]. However, it is worth noted that in the latter part of Li deposition in the second cycle, a second plateau with the potential similar to the deposition overpotential in the first cycle appeared. It is suggested that the first and second plateau is ascribed to the newly deposited Li (HSAL) stripping and the bulk (original) Li, which is covered by the thick SEI due to the low reduction potential of metallic Li, stripping on the Li side, respectively. Thus, the overpotential relates to Li deposition/dissolution processes on the Li surface is significantly influenced by the nature of SEI, the HSAL on both Cu, Li surfaces, and the charge transfer processes at both interfaces.

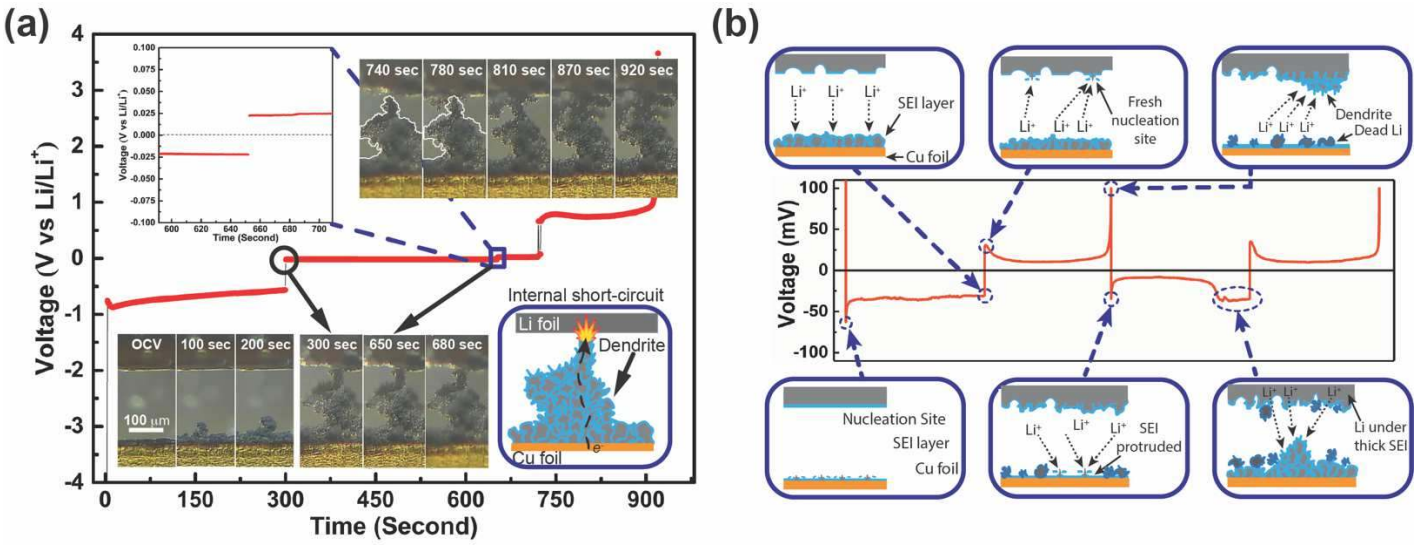

Fig. 1 *In-situ* OM and Li deposition/dissolution scheme. **a**, *In-situ* OM measurement of Li deposition/dissolution on Cu electrode under ultra-high current density of 500 mA cm^{-2} for demonstration of short-circuit. **b**, Scheme of Li deposition/dissolution on Cu foil during cycling of Li//Cu cell under current density of 0.2 mA cm^{-2}.

Proposed integrated protocol. In this section, the four types of cell configuration as an integrated protocol assembled by Li//Li symmetric cell, Li//Cu cell, cathode/Li cell, and cathode/Cu anode-free cell was applied to comprehensively evaluate the performance of LMBs/AFLMBs and unravel the unseen messages concealed in the individual candidates. Fig. 2 shows the charge/discharge profiles of all the cell configuration used in the protocol. Fig. 3 shows the proposed integrated protocol and the schematics of each

cell configuration at its fully charged and discharged state. From the integrated protocol, one can decrypt different information from each cell set-ups and dissect the origins of irreversible coulombic efficiency (irr-CE) and capacity within LMB/AFLMB quantitatively.

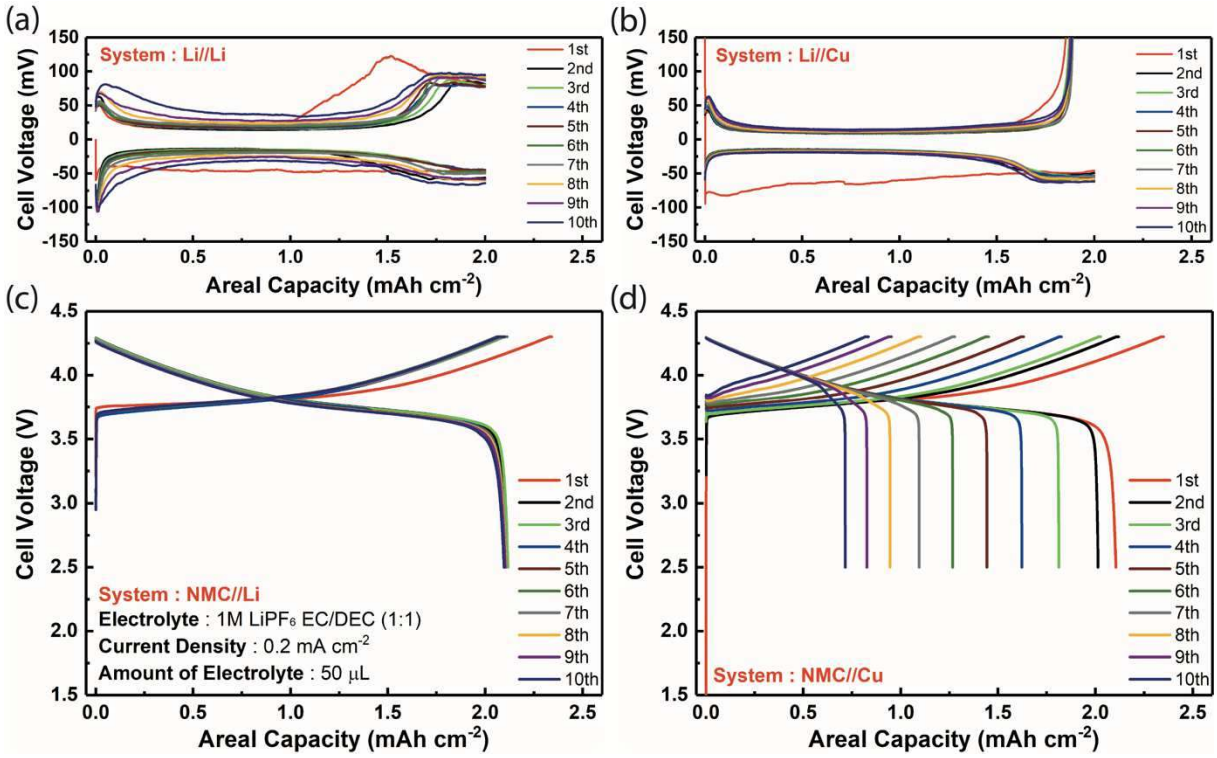

Fig. 2 Electrochemical charge and discharge curves. **a**, Li//Li. **b**, Li//Cu. **c**, NMC//Li. **d**, NMC//Cu. All the cells use 1M $LiPF_6$ in EC/DEC (1:1) as electrolyte with the current density of 0.2 mA cm^{-2}. We selected NMC-111 as the cathode material used in this electrolyte, one can substitute desired cathode material for cathode study in cathode/Li cell and AFLMB.

Li//Li symmetric cell, with its charge/discharge curves shown in Fig. 2a, is a useful configuration that allows us to understand the kinetics of Li deposition/dissolution by extracting the initial nucleation overpotential and polarization information[11, 28, 30]. It is also a powerful tool to investigate internal short circuit (ISC), critical current density (CCD) phenomenon, or SEI polarization on Li surface which although depends on the surface quality of both Li electrodes. However, irr-CE is unable to be obtained from Li//Li cell since the CE is always ~100% due to excess Li from both Li electrodes which compensate the formation of dead Li and active Li lost from reductive electrolyte decomposition (SEI formation or gas generation). As a result, the consumption of active Li due to the aforementioned reactions is invisible, thus, seldom discussed and often overlooked in this cell configuration[4]. Generally, it is not easy to report reliable and reproducible information on cycling performance or even ISC of this Li//Li protocol unless the quality of Li surface employed, the amounts of electrolytes, and the pressure on the tested cell are well-controlled.

However, by replacing Li with Cu as the working electrode in Li//Cu cell as shown in Fig. 2b, it is possible to quantify the active Li consumption at the Cu electrode by splitting out the proportion of irr-CE contributed from reductive electrolyte decomposition and the formation of dead Li in each cycle, respectively. Fig. 3a and 3b show the scheme of Li//Cu cell at fully plated and stripped state in the 1st cycle. In the Li//Cu cell, since the excess Li is from the Li electrode, resulting in the Cu side as the limiting electrode. Since there is no excessive metallic Li on Cu as it was in Li//Li cell to compensate the irreversible consumption of active Li on Cu. The irreversible phenomena observed mainly reflect the behaviors of the Cu electrode. In general, the irr-CE of Li//Cu cell is higher in the 1st cycle containing both SEI formation via reductive electrolyte decomposition and dead Li formation. Although there still exists a slight contribution from the SEI fracture in the subsequent cycles[29], it is mainly contributed to dead Li formation (green bar in Fig. 3g) after the formation of a stable SEI in the 1st cycle, especially at low C-rate. Therefore, the irr-CE originated from the reductive electrolyte decomposition (red bar in Fig. 3g) can be calculated by subtracting the value in the 1st cycle with that of the 2nd cycle from the Li//Cu cell protocol, and the useful information of irr-CE from the dead lithium formation and reductive electrolyte decomposition can be successfully extracted from the Li//Cu protocol as shown in Fig. 3g. The Li//Cu cell is a useful protocol to provide reliable

information for the study of electrolyte[23, 24, 27], and surface engineering approaches[25, 31, 32] for mitigating the irreversible Coulombic efficiency ascribed to dead Li formation and reductive electrolyte decomposition.

The third protocol is a cathode//Li cell and the charge /discharge curves are shown in Fig. 2c, namely a half-cell for studying phenomena taking place at the cathode. When the cathode//Li cell is fully charged, Li^+ is de-intercalated from NMC and plated onto the Li anode along with the formation of dendritic or mossy Li (Fig. 3c). In reverse, Li^+ is stripped from the Li anode with some dead Li left on it and intercalated back into NMC (Fig. 3d). However, since there is a great amount of active Li on the Li electrode compared to that in the cathode electrode, i.e. the capacity ratio of the anode to cathode (A/C) is > 1 and cathode is the limiting electrode, the excess metallic Li will compensate the active Li loss due to dead Li formation and reductive electrolyte decomposition at the anode side, leading them invisible from the irr-CE observed. Since the irreversible reactions at the anode cannot be observed, this protocol acts as an efficient tool to extract information relating to the irreversible reactions at the cathode including oxidative electrolyte decomposition, cathode degradation, and 1st intrinsic irreversible capacity of cathode material in the 1st cycle[33, 34, 35, 36, 37]. Generally, the irr-CE of cathode//Li cells in the 1st cycle is often found larger due to the cathode-electrolyte interphase (CEI) formation and additional side reactions than that in the subsequent cycles. In particular, this phenomenon is more significant and often observed in layered oxide cathode materials which can be attributed to mainly the slow lithium kinetics at high lithium contents and partially the formation of Li_2MO_2-like phases, and this intrinsic irr-capacity cannot be recovered in the absence of deep discharge of the cell or unless cycling at the higher temperature to eliminate the kinetics limitation[33, 34, 35]. As for the subsequent cycles, the degradation of cathode materials itself plays an important role in the following capacity fading. Besides, the oxidative electrolyte decomposition in the subsequent cycles at high voltage may also generate irr-CE but less significant compared to the 1st cycle. Based on the above mentioned three origins of irr-CE at the cathode, by transferring the irr-CE of 2nd cycle to that in 1st cycle, which is originated from the oxidative electrolyte decomposition and the cathode degradation (blue bar in Fig. 3g), denoted as subsequent irreversible reactions at the cathode (sub. irr-rxn at the cathode), it is possible to extract out the amount of irr-CE owing to the 1st intrinsic irr-capacity of the layered oxide cathode together with the loss from CEI formation (shown in the yellow-gray alternating bar in Fig. 3g). Thus, from the bar plot of cathode//Li cell in Fig. 3g, the irr-CE can be quantitively separated into the 1st intrinsic irr-capacity of the layered cathode together with the irr-CE from the CEI formation and sub. irr-rxn at the cathode, respectively. If a deep discharge is performed in the 1st cycle, the 1st irr-capacity, capacity loss from CEI formation, and the sub. irr-capacity can be discerned from the cathode//Li protocol (see Fig. S2).

The cathode//Cu cell, which is also called AFLMB as displayed in Fig. 2d, can be recognized as a full cell with the A/C ratio ≅ 1 since the active Li is purely from the cathode. The two half-reactions taking place in the AFLMB are comparable to those in cathode//Li and Li//Cu cells, namely Li deposition/dissolution on Cu and cathode oxidation/reduction, respectively. When the anode-free cell is fully charged, Li^+ is de-intercalated from NMC and plated onto the Cu along with the formation of dendritic or mossy Li (Fig. 3e). In reverse, Li^+ is stripped from the anode with some dead Li left on Cu and intercalated back into NMC (Fig. 3f). Therefore, the irreversible capacity and CE of AFLMB are significantly relative to that of Li//Cu and cathode/Li cells, and by integrating the information of Li//Cu and cathode/Li cells, it is possible to dissect the proportion of irreversible capacity and CE in anode-free cells generated from different origins as shown in Fig. 3g and will be discussed in the following paragraphs.

Since the capacity of anode and cathode changes along with the cycles in an AFLMB, its A/C ratio and limiting electrode will also change, which will affect the analysis of the contribution of irr-CE. Therefore, it is important to know how the capacity changes in both electrodes. From the perspective of capacity, if the cathode material used possesses the 1st intrinsic irr-capacity of layered oxide cathode, excess active Li would be left on Cu in the form of metallic Li causing the A/C ratio > 1 and cathode as limiting electrode after the 1st cycle, causing the irr-CE of AFLMB only contributed from the cathode as that in an NMC//Li cell, and generating high coulombic efficiency. In contrast, the irr-capacity of AFLMB will be only ascribed to the anode if the A/C ratio becomes < 1. Additionally, since the irr-capacity caused by the subsequent irreversible reactions at the cathode is significantly low compared to dead Li formation, the observed reversible (active) capacity of AFLMB can serve as an indication to the *in-situ* A/C ratio of the cell.

To study the effect of capacity retention on AFLMBs and LMBs, Fig. S3, and Fig. S4 show the charge/discharge profiles and cycling performance results of NMC//Li cells with different A/C ratio. When the reversible capacity is kept almost the same to that of the 1st cycle discharge capacity as if in cathode//Li cell, it can be reckoned as the A/C ratio is > 1 where all the irr-capacity observed arouses from the cathode. (see Fig. S4b) However, the hidden chemistry beneath this phenomenon is the continued consumption of excess Li. This is because dead Li forms in each cycle, yet, since the active Li inventory within AFLMB cells is solely provided by the cathode and limited, thus, it is continuously being consumed as shown in Fig. S4a.

During the continuous consumption of active Li inventory, there will be a transition state in a specific cycle when the A/C ratio is about to become < 1. From Fig. S4b, this unique circumstance can be characterized by a sudden fading slope transition of the discharge capacity of AFLMB, implying the excess Li is no longer enough to compensate dead Li formation in each cycle, which leads to less active Li at the anode than that at cathode, limiting the observed reversible capacity of AFLMB as shown in Fig. 3g. Therefore, the irr-CE observed will be the combination of both anode and cathode in transition state and dominated by dead Li formation afterwards. As a result, the poor CE and significant capacity fading in the subsequent cycles of AFLMBs are mainly caused by the formation of dead Li that could not be stripped back to cathode. To conclude, the larger the A/C ratio and less severe dead Li formation, the later the transition state is occurred as shown in Fig. S4b. Thus, by enhancing the CE of Li plating/stripping and suppressing dead Li formation, the capacity retention and the high CE region can be improved and prolonged in AFLMBs, respectively.

Given irr-CE, the irr-CE induced from dead Li formation and reductive electrolyte decomposition can be first quantified through transferring the information from Li//Cu cell. Secondly, the proportion of irr-CE from the sub. irr-rxn at the cathode can be dissected referring to the 2nd cycle irr-CE of cathode//Li cell. Finally, if the cathode material used processes the 1st intrinsic irr-capacity and CEI formation, the contribution of them can also be computed after separating that of sub. irr-rxn at the cathode from cathode//Li cell. Moreover, oxidative electrolyte decomposition at the cathode side would also lead to the supply of additional active Li inventory plated on Cu as the counter reduction reaction. Therefore, the partial consumption of active Li from the dead Li formation during the discharge process may also be compensated by this irreversible reaction at the cathode. Considering the effect of A/C ratio on irr-CE, when the A/C ratio is > 1, the proportion of irr-CE from the anode is not observable and plotted in the light color bar with a dashed outline in Fig. 3g. When the in the transition state, some of the irr-CE from dead Li formation will be compensated by excess Li as shown in the brown bar in Fig. 3g. Lastly, when the A/C ratio < 1, the irr-CE of AFLMB is mainly dominated by dead Li formation.

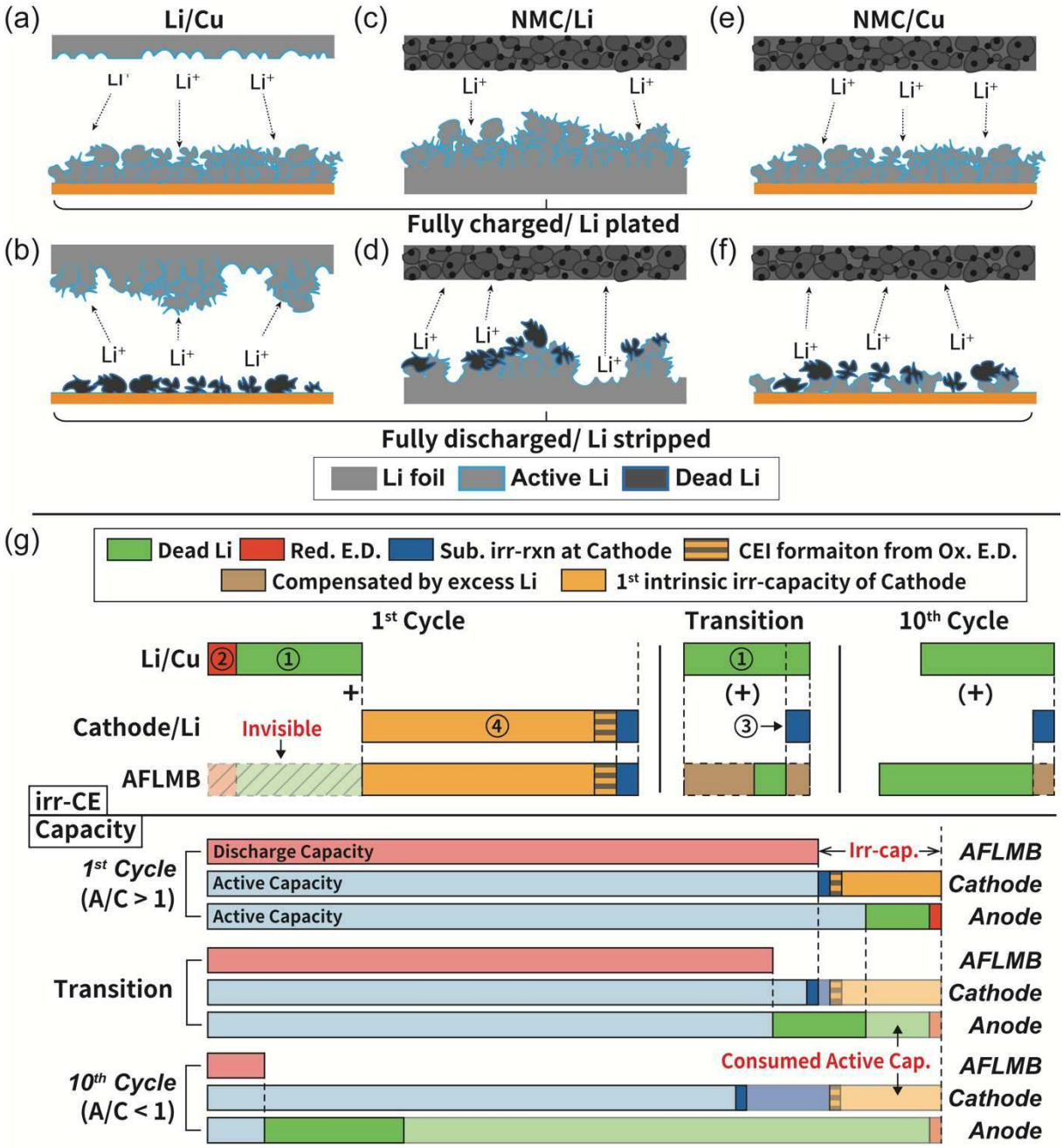

Fig. 3 Integrated protocol and scheme of different cell configuration at fully charged and discharged states. **a**, **b, c,** Scheme of Li//Cu, NMC//Li, and NMC//Cu cells at fully charged/ Li pated sate in the first cycle, respectively. **d**, **e**, **f**, Scheme of Li//Cu, NMC//Li, and NMC//Cu cells at fully discharge/ Li stripped state in the first cycle, respectively. **g**, Proposed integrated protocol to unravel the origins of irreversible CE in AFLMB by Li//Cu and cathode/Li cells. The blue shell on Li represents the SEI layer. Red. E.D. stands for the reductive electrolyte decomposition, Ox. E.D. for oxidative electrolyte decomposition, and sub. irr-rxn for subsequent irreversible reactions, respectively.

Example 1: 1M $LiPF_6$ in EC:DEC under 0.2 mA cm^{-2}. Fig. 4 shows the corresponding irreversible CE at the 1st, the 2nd, and the 10th cycle of Li//Cu, NMC//Li, and NMC//Cu cells under the current density of 0.2 mA cm^{-2} in commercial electrolyte (1M $LiPF_6$ in EC:DEC). From the result obtained from the integrated protocol, the irr-CE of the 1st and the 2nd cycle of Li//Cu cell is 5.73% and 5.48%, respectively, suggesting the 0.25% higher irr-CE than 2nd cycle is mainly caused by the reductive electrolyte decomposition, where the rest of ~5.48% can be considered as dead Li formation based on the approaches discussed in Fig. 3g. For cathode//Li cell (Fig. 2a) with A/C = 50, the irr-CE of 1st cycle is 10.36% containing 9.46% of the 1st intrinsic irr-capacity of cathode with CEI formation and 0.9% of subsequent irreversible reactions at cathode. In addition, it should be stated that the cycling performance of NMC//Li is only independent of Li when the amount of active Li is sufficient enough with low charge/discharge rate. When increasing the current

density to 0.4 mA cm^{-2}, it is found that the capacity is declining quickly due to the cathode degradation induced from soft short-circuit (SSC) and severe dendrite formation, as shown in Fig. S6 and Fig. S7.

NMC//Cu cell shows the highest initial overpotential among all the cell configuration, which can be attributed to the higher initial Li nucleation barrier on Cu than on Li and charge transfer resistance of NMC cathode. Interestingly, the polarization at 50% stats-of-charge (SOC) of NMC//Cu is lower than that of NMC//Li, as shown in Fig. S8a. This can be explained by the lower mass transport resistance through thin SEI on Cu than thick SEI on Li due to the intrinsically-reactive nature of Li. This phenomenon is also seen between Li//Li and Li//Cu cells. From the integrated protocol, the 1st cycle irr-CE of NMC//Cu (AFLMB) cell is comparable to NMC//Li cell and can be also separated into 9.5% of 1st intrinsic irr-capacity of NMC with CEI formation and 0.9% of subsequent irreversible reactions at cathode since the A/C ratio is currently > 1 and the cathode is the limiting electrode, making the irr-CE from anode invisible. In the 2nd cycle, the irr-CE is decreased to 4.48%, with the contribution mainly from dead Li formation as the cell is in the transition state to A/C < 1 and the irr-capacity and CE are limited by the anode. However, the higher irr-CE of AFLMB than Li//Cu cell in the 10th cycle may due to more complicated cell chemistry involving dead Li formation or chemical crossover effect[38]. Yet, it can still be concluded that dead Li formation is no doubt the greatest obstacle currently for the development of high-performance AFLMBs.

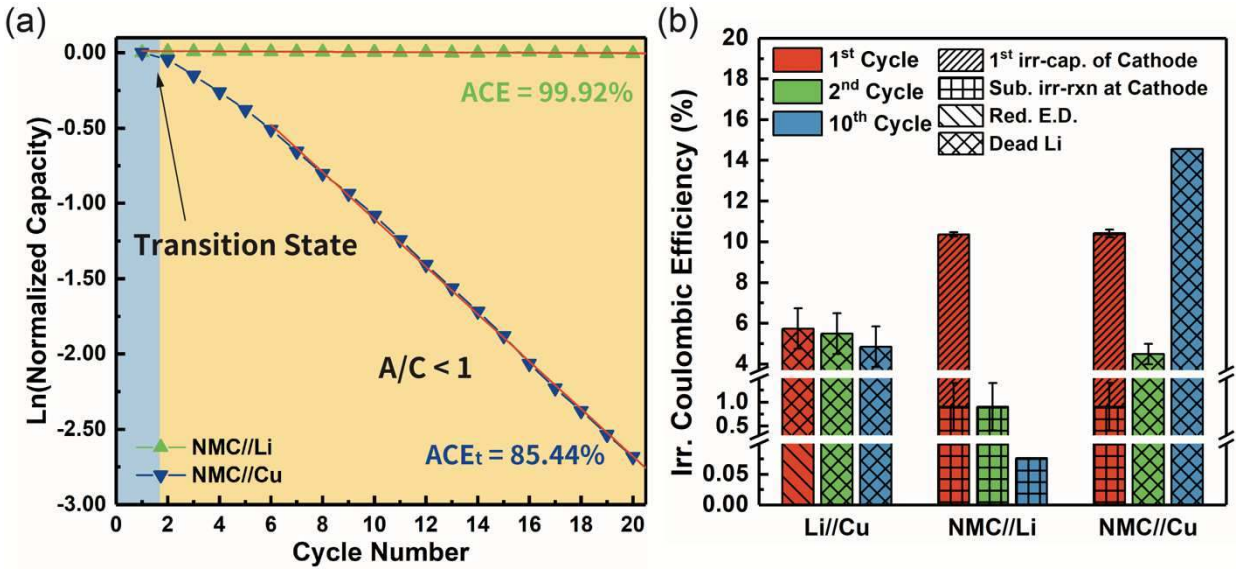

Fig. 4 Results obtained from integrated protocol using 1M $LiPF_6$ in EC/DEC (1:1) as electrolyte under 0.2 mA cm^{-2}. **a**, Normalized discharge capacity versus cycle number of NMC//Li and NMC//Cu cells. **b**, irreversible CE comparison of four cell set-ups using 1M $LiPF_6$ in EC/DEC (1:1) as electrolyte with the current density of 0.2 mA cm^{-2}. NMC-111 electrode with an areal capacity of ~2 mAh cm^{-2} was used as the cathode electrode for demonstration in this work. The 10th cycle irr-CE of NMC//Li and NMC//Cu cells shown here and for the rest of the examples in this work are the average irr-CE extracted from the linear fitted results of ln(normalized capacity) versus cycle number to present a more general and reliable irr-CE. It should be noted the average irr-CE of NMC//Cu cell is calculated after transition state, namely in the region of A/C ratio < 1. The capacity retention comparison of NMC//Li and NMC//Cu cells are shown in Fig. S5a.

Experimental validation for the proposed protocol. Since dead-Li formation is the major origin of irr-CE in AFLMB as mentioned above and to further validate the reliability of the results obtained from the proposed protocol, the amount of dead-Li at different cycles of AFLMBs and Li//Cu cells at their Li-stripped state is measured using the methods reported by Meng et al.[39] and compared with the values dissected from the protocol as shown in Fig. 5. It is observed that in Li//Cu cell, the deduction of the 1st reductive electrolyte decomposition from the 1st cycle irr-CE is close to the dead-Li obtained by titration gas chromatography (TGC) method, which confirms the reliability of our proposed protocol for quantifying the origins of irr-CE in Li//Cu cell. However, it should be noted that since the SEI fracture and formation would continue to occur in the subsequent cycles due to the unstable property of the as-formed SEI and dendrite formation[29]. Thus, the SEI feature and formation consume dead-Li and cause less detected value when using the TGC method for quantifying dead-Li amount in the subsequent cycles.

Meanwhile, it should be noted that for the validation of NMC//Cu cells, Li^0 is used to represent the origin of the obtained value from the TGC method instead of dead-Li since the presence of excess active Li after the 1st cycle of AFLMB left on Cu which is not truly "dead". From the results shown in Fig. 5, there is also a discrepancy between the total irr-CE value and the sum of 1st reductive electrolyte decomposition and Li^0 amount from the TGC method. This difference could originate from both electrochemically oxidative and chemically reductive electrolyte decomposition in the 1st cycle of the NMC//Cu cell, respectively. As in the 2nd and 10th cycles, the increased discrepancy between the total irr-CE value and that of measured by the TGC method can be again explained by the continuous SEI evolution in the subsequent cycles like in Li//Cu cells. To conclude, the amount of dead-Li in the 1st cycle of Li//Cu cell and the dead-Li accumulation trend in both Li//Cu and AFLMB cells obtained from our proposed protocol is successfully validated by the TGC method. However, by examining the proposed protocol, we could not only easily quantify the actual amount of dead-Li excluding the potential discrepancy from the chemical side reaction between dead-Li and electrolyte but also deduct the portion of irr-CE from other origins in AFLMBs, which provides a more comprehensive understanding of AFLMBs. Hence, for further evaluation of the protocol under different circumstances, two example studies are conducted by changing the current density and electrolyte formulation in the following sections, respectively.

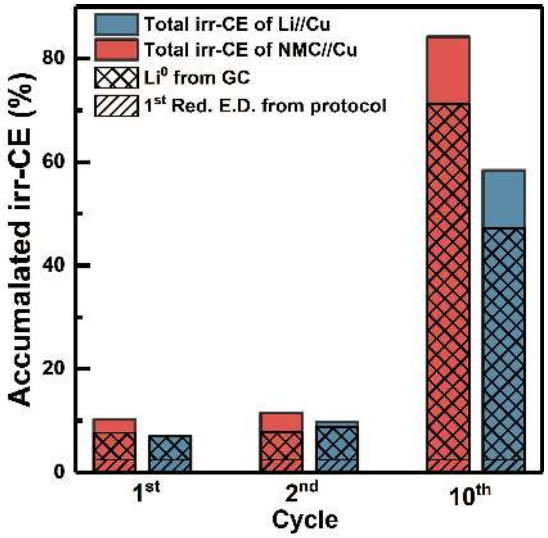

Fig. 5 Dead-Li validation for the irr-CE obtained from the proposed protocol using the titration gas chromatography method.

Example 2: 1M $LiPF_6$ in EC:DEC under 0.4 mA cm^{-2}. The effect of current density is also studied using the integrated protocol. Fig. 6 shows the obtained results using the same electrolyte from the previous section but under a current density of 0.4 mA cm^{-2}. The 1st, 2nd, and 10th cycle irr-CE of Li//Cu cell are 7.5%, 6.2%, and 8.6%, respectively, representing 1.3% of reductive electrolyte decomposition on Cu with 6.2% of dead Li formation in the 1st cycle and mainly dead Li formation in the subsequent cycles. While the irr-CE of 11.19% for NMC//Li cell in the 1st cycle can be attributed to the combination of 10.62% 1st intrinsic irr-capacity of NMC and 0.57% subsequent irreversible reactions at cathode transferred from 2nd cycle. Therefore, after integrating the results from Li//Cu and NMC//Li cells, the irr-CE of NMC//Cu cell in the 1st cycle can be summarized as 10.62% 1st intrinsic irr-capacity of NMC and 0.57% subsequent irreversible reactions at the cathode as A/C ratio is larger than one and the determining electrode is the cathode. In the 2nd cycle, the irr-CE is significantly larger than that in 0.2 mA cm^{-2}, this can be explained by the increased dendritic and dead Li formation rate under higher current density. Thus, the contribution of dead Li formation in irr-CE is higher and consumes more amount of excess Li in each cycle, causing the faster transition to A/C < 1 and higher irr-CE of the 2nd cycle than 0.2 mA cm^{-2}. However, in the 10th cycle of NMC//Cu, the major origin of irr-CE is still the dead Li formation no matter the current density after the A/C ratio is < 1.

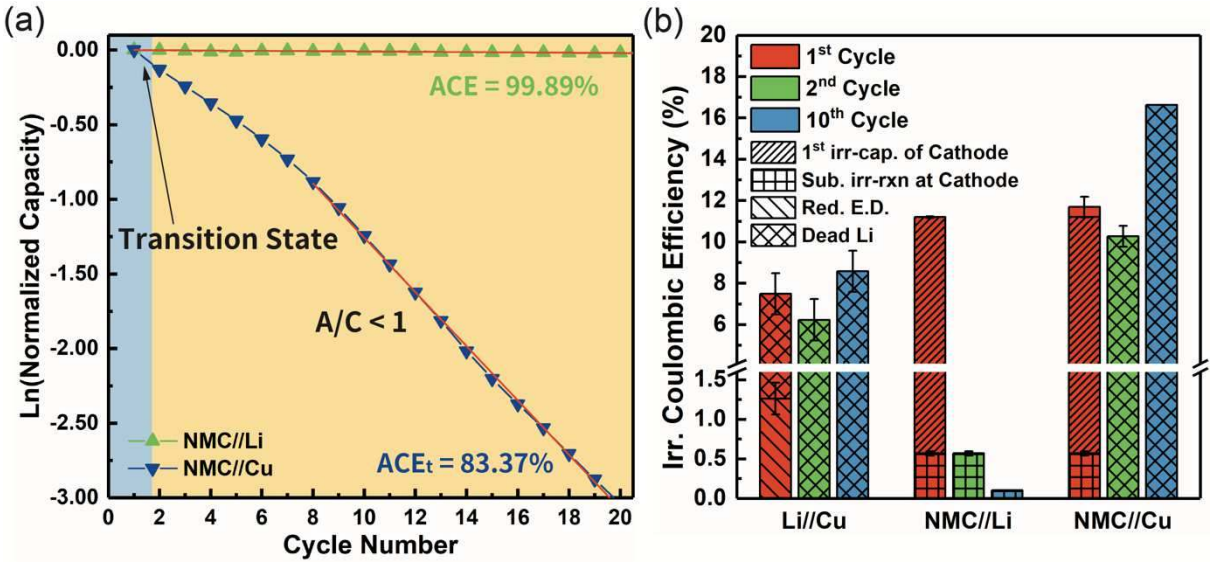

Fig. 6 Results obtained from integrated protocol using 1M $LiPF_6$ in EC/DEC (1:1) as electrolyte under 0.4 mA cm^{-2}. **a**, Normalized discharge capacity versus cycle number of NMC//Li and NMC//Cu cells. **b**, irreversible efficiency comparison of four cell set-ups using 1M $LiPF_6$ in EC:DEC as electrolyte with the current density of 0.4 mA cm^{-2}. The capacity retention comparison of NMC//Li and NMC//Cu cells are shown in Fig. S5b. The charge/discharge profiles of each cell configuration are shown in Fig. S9.

Example 3: 1M $LiPF_6$ in EC:DEC with 5% FEC. Fig. 7 shows the results obtained from the integrated protocol using 1M $LiPF_6$ in EC:DEC with 5% FEC as the electrolyte under the current density of 0.2 mA cm^{-2}. The 1st and 2nd cycle irr-CE of Li//Cu is 4% and 2.9%, respectively. Similar to the previous case, the 1.1% difference can be attributed to the reductive electrolyte decomposition on Cu in the 1st cycle and the rest 2.9% can be attributed to dead Li formation. From the result of Li//Cu cell, the effect of FEC on suppressing dead Li and dendrite formation can already be revealed from the lower irr-CE than that of without FEC additive. Meanwhile, the irr-CE of NMC//Li cell in 1st cycle can be separated into the 1st intrinsic irr-capacity of NMC and CEI formation (9.72%) and subsequent irreversible reactions at cathode (0.31%) including oxidative electrolyte decomposition and cathode degradation transferred from 2nd cycle. Finally, the irr-CE of NMC//Cu in the 1st cycle, same with that of NMC//Li cell, can be broken down to 9.72% of the 1st intrinsic irr-capacity of NMC with CEI formation and 0.31% of subsequent irreversible reactions at cathode when the A/C ratio > 1. However, the irr-CE of the 2nd cycle is 0.52% and significantly lower than that in the NMC//Cu cell without FEC added. This can be again explained by the effect of FEC suppressing dead Li formation, leading to slower consumption of excess active Li on Cu. Thus, the A/C ratio of the cell is sustained > 1 longer than that without FEC additive before transiting to A/C < 1 as discussed above, and the irr-CE of the first four cycles is very low as shown in Fig. 7a. In other words, the transition state is delayed to the 5th cycle. Meanwhile, the discharge capacity is found without decaying in the first four cycles, which also proves that the A/C > 1 region is extended to four cycles. As a result, the irr-CE of the 2nd cycle is mainly due to the subsequent irreversible reactions at cathode considering cathode is still the limiting electrode, different from those without FEC added. Later on, after the transition state and the A/C becomes < 1, the increased average irr-CE of 3.1% can be thus attributed to the dead Li formation.

To conclude, if we compare the results obtained from the proposed protocol between with/without FEC as an additive, the lower initial overpotential, and polarization shown by Li//Li and Li//Cu cells after the introduction of FEC reveals the effect of FEC on forming better SEI and favoring Li nucleation on Cu. The lower irr-CE of Li//Cu cell and significantly lower irr-CE after the 1st cycle in NMC//Cu (AFLMB) cell indicate the ability of FEC to suppress dendrite and dead Li. Interestingly, the irr-CE of NMC//Li cell does not show significant difference with/without FEC suggesting the contribution of FEC is less notable for the cathode. Although it has been reported that the addition of FEC into electrolytes can lead to a more compacted and stable LiF-rich SEI, which is also beneficial to the uniform Li deposit and better electrochemical perofrmance[40]. By summarizing all the contributions from the above configuration within the proposed protocol, we can quantitively unravel the effects of FEC on mitigating the formation of dead Li and forming stable SEI in AFLMB.

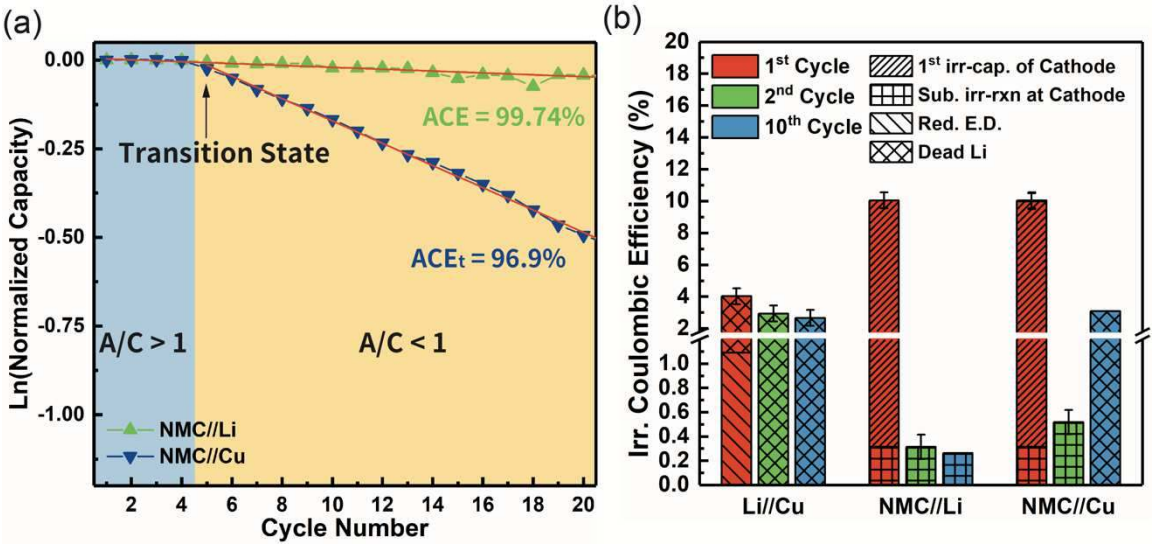

Fig. 7 Results obtained from integrated protocol using 1M $LiPF_6$ in EC/DEC (1:1) with 5% FEC added as electrolyte. **a**, Normalized discharge capacity versus cycle number of NMC//Li and NMC//Cu cells. **b**, irreversible CE comparison of four cell set-ups using 1M $LiPF_6$ in EC/DEC (1:1) with 5% FEC added as electrolyte with the current density of 0.2 mA cm^{-2}. The capacity retention comparison of NMC//Li and NMC//Cu cells are shown in Fig. S5c. The charge/discharge profiles of each cell configuration are shown in Fig. S10.

Discussion

In summary, we revealed the formation of dead Li and dendritic Li alongside with the internal short-circuit via *in-situ* OM, and proposed the mechanism of Li deposition/dissolution on Cu. Furthermore, by combining the information and irreversible coulombic efficiency of four different cell set-ups, an integrated protocol is proposed to unravel the concealed messages of various irreversible Coulombic efficiency. From the decrypted information, the origin and proportion of irreversible coulombic efficiency in AFLMBs induced from dead Li formation, reductive/oxidative electrolyte decomposition, 1st intrinsic irreversible capacity of the cathode, and cathode material degradation can be quantified and revealed. Although AFLMBs suffer from high irreversible coulombic efficiency and quick capacity fading and often recognized as a poor cell configuration, AFLMB is the indispensable key in this integrated protocol to facilitate the development of electrolyte and improve the performance of LMB and AFLMB, just like a rose always has its thorns. In general, the integrated protocol proposed here can be further expanded to comprehensively examine the effectiveness of various strategies on improving the electrochemical performance of LMBs or AFLMBs, to realize next-generation high energy rechargeable lithium battery involving metal deposition/stripping chemistry.

Methods

Materials

The commercial NMC electrodes (Amita Technologies Inc. Taiwan) contain 88.5 wt% of active material ($LiNi_{1/3}Co_{1/3}Mn_{1/3}O_2$, NMC-111), 4 wt% of polyvinylidene fluoride binder (PVDF), and 7.5 wt% of conductive carbon (2.5 wt% of Super P with 5 wt% of KS6). The nominal areal discharge capacity of NMC electrodes used is 2 mAh cm^{-2}.

Cu foil was used as an anode electrode in the anode-free cell. The Cu foil was cut into 19 mm in diameter, washed by 1M hydrochloric acid for 10 minutes in an ultrasonic cleaner, followed by rinsing with deionized water and acetone for three times, and finally vacuumed in the desiccator for 30 minutes before use.

Cell Assembly

The optical microscopy (OM) Li//Cu cell was assembled by sealing a Li foil and copper foil with a distance around 250 μm in-between inside a plastic pouch cell. Copper wire was used as terminal for both electrodes and external circuit for electrochemical measurements. The OM cells and CR2032 coin cells were all assembled in an argon-filled glovebox (UNIlab Plus Glove Box, MBRAUN) where the oxygen and moisture content were kept less than 1 ppm.

Li foil (~300 μm, FMC Corporation) was attached on a 500 μm spacer and used as an anode in NMC//Li cell, identical electrodes in Li//Li symmetric cell, and tri-layer Celgard 2325 PP/PE/PP membrane as separator. The NMC//Cu cells were assembled by pairing NMC electrode with a copper foil, with a 800 μm spacer to minimize the thickness difference of assemblies within in the cell between NMC//Cu and NMC//Li cells to unify the cell pressure and make the results obtained from each cell configuration the most reliable. The electrolyte used was 1M lithium hexafluorophosphate ($LiPF_6$) in the mixture of ethylene carbonate (EC) and diethyl carbonate (DEC) (v:v = 1:1) (Sigma-Aldrich) with or without 5% of fluoroethylene carbonate (FEC).

***In-situ* Optical Microscopy Observation**

In-situ plating and stripping of Li on copper foil was observed using optical microscopy (OM) in a plastic pouch cell by applying 500 mA cm^{-2} of charge/discharge current density, as shown in Fig. 1a and the movies are also included in the supporting information. The electrochemical measurement of the cell was simultaneously conducted on a PGSTAT101 Autolab potentiostat (Metrohm), with the potential and current resolution of 3 μV and 10 nA, respectively.

Electrochemical Tests

Galvanostatic charge/discharge was used to cycle batteries with applied current density of either 0.2 or 0.4 mA cm^{-2} to study the effect of charge/discharge rate. Galvanostatic charge/discharge tests were performed on Arbin BT-2000 (Arbin Instruments) battery test equipment at room temperature.

References

1. Armand M, Tarascon JM. Building better batteries. *Nature* **451**, 652-657 (2008).
2. Tarascon JM, Armand M. Issues and challenges facing rechargeable lithium batteries. *Nature* **414**, 359-367 (2001).
3. Li S, Jiang M, Xie Y, Xu H, Jia J, Li J. Developing High-Performance Lithium Metal Anode in Liquid Electrolytes: Challenges and Progress. *Adv Mater* **30**, e1706375 (2018).
4. Cheng J-H*, et al.* Visualization of Lithium Plating and Stripping via in Operando Transmission X-ray Microscopy. *The Journal of Physical Chemistry C* **121**, 7761-7766 (2017).
5. Jiao S*, et al.* Behavior of Lithium Metal Anodes under Various Capacity Utilization and High Current Density in Lithium Metal Batteries. *Joule* **2**, 110-124 (2018).
6. Liu B, Zhang J-G, Xu W. Advancing Lithium Metal Batteries. *Joule* **2**, 833-845 (2018).
7. Xu W*, et al.* Lithium metal anodes for rechargeable batteries. *Energy Environ Sci* **7**, 513-537 (2014).
8. Lin D, Liu Y, Cui Y. Reviving the lithium metal anode for high-energy batteries. *Nat Nanotechnol* **12**, 194-206 (2017)
9. Cheng XB, Zhang R, Zhao CZ, Zhang Q. Toward Safe Lithium Metal Anode in Rechargeable Batteries: A Review. *Chem Rev* **117**, 10403-10473 (2017).
10. Haregewoin AM, Wotango AS, Hwang B-J. Electrolyte additives for lithium ion battery electrodes: progress and perspectives. *Energy Environ Sci* **9**, 1955-1988 (2016).
11. Ryou M-H, Lee YM, Lee Y, Winter M, Bieker P. Mechanical Surface Modification of Lithium Metal: Towards Improved Li Metal Anode Performance by Directed Li Plating. *Advanced Functional Materials* **25**, 834-841 (2015).
12. Zheng J*, et al.* Highly Stable Operation of Lithium Metal Batteries Enabled by the Formation of a Transient High-Concentration Electrolyte Layer. *Advanced Energy Materials* **6**, 1502151 (2016).
13. Tripathi AM, Su WN, Hwang BJ. In situ analytical techniques for battery interface analysis. *Chem Soc Rev* **47**, 736-851 (2018).
14. Choi JW, Aurbach D. Promise and reality of post-lithium-ion batteries with high energy densities. *Nature Reviews Materials* **1**, (2016).

15. Xu R*, et al.* Artificial Interphases for Highly Stable Lithium Metal Anode. *Matter* **1**, 317-344 (2019).
16. Pang Q, Liang X, Shyamsunder A, Nazar LF. An In Vivo Formed Solid Electrolyte Surface Layer Enables Stable Plating of Li Metal. *Joule*, (2017).
17. Chen S*, et al.* Critical Parameters for Evaluating Coin Cells and Pouch Cells of Rechargeable Li-Metal Batteries. *Joule* **3**, 1094-1105 (2019).
18. Wang J*, et al.* Improving cyclability of Li metal batteries at elevated temperatures and its origin revealed by cryo-electron microscopy. *Nature Energy* **4**, 664-670 (2019).
19. Louli AJ, Ellis LD, Dahn JR. Operando Pressure Measurements Reveal Solid Electrolyte Interphase Growth to Rank Li-Ion Cell Performance. *Joule* **3**, 745-761 (2019).
20. Niu C*, et al.* High-energy lithium metal pouch cells with limited anode swelling and long stable cycles. *Nature Energy* **4**, 551-559 (2019).
21. Liu J*, et al.* Pathways for practical high-energy long-cycling lithium metal batteries. *Nature Energy* **4**, 180-186 (2019).
22. Qian J*, et al.* Anode-Free Rechargeable Lithium Metal Batteries. *Advanced Functional Materials* **26**, 7094-7102 (2016).
23. Hagos TM*, et al.* Dual electrolyte additives of potassium hexafluorophosphate and tris (trimethylsilyl) phosphite for anode-free lithium metal batteries. *Electrochimica Acta* **316**, 52-59 (2019)
24. Beyene TT*, et al.* Concentrated Dual-Salt Electrolyte to Stabilize Li Metal and Increase Cycle Life of Anode Free Li-Metal Batteries. *Journal of the Electrochemical Society* **166**, A1501-A1509 (2019).
25. Assegie AA, Chung C-C, Tsai M-C, Su W-N, Chen C-W, Hwang B-J. Multilayer-graphene-stabilized lithium deposition for anode-Free lithium-metal batteries. *Nanoscale* **11**, 2710-2720 (2019).
26. Weber R*, et al.* Long cycle life and dendrite-free lithium morphology in anode-free lithium pouch cells enabled by a dual-salt liquid electrolyte. *Nature Energy* **4**, 683-689 (2019).
27. Hagos TT*, et al.* Locally Concentrated LiPF6 in a Carbonate-Based Electrolyte with Fluoroethylene Carbonate as a Diluent for Anode-Free Lithium Metal Batteries. *ACS Applied Materials & Interfaces* **11**, 9955-9963 (2019).
28. Burns JC*, et al.* Introducing Symmetric Li-Ion Cells as a Tool to Study Cell Degradation Mechanisms. *Journal of The Electrochemical Society* **158**, (2011).
29. Thirumalraj B*, et al.* Nucleation and Growth Mechanism of Lithium Metal Electroplating. *J Am Chem Soc* **141**, 18612-18623 (2019).
30. Gao J*, et al.* Lithiated Nafion as polymer electrolyte for solid-state lithium sulfur batteries using carbon-sulfur composite cathode. *Journal of Power Sources* **382**, 179-189 (2018).
31. Assegie AA, Cheng JH, Kuo LM, Su WN, Hwang BJ. Polyethylene oxide film coating enhances lithium cycling efficiency of an anode-free lithium-metal battery. *Nanoscale* **10**, 6125-6138 (2018).
32. Abrha LH*, et al.* Li7La2.75Ca0.25Zr1.75Nb0.25O12@LiClO4 composite film derived solid electrolyte interphase for anode-free lithium metal battery. *Electrochimica Acta* **325**, (2019).
33. Kang S-H, Yoon W-S, Nam K-W, Yang X-Q, Abraham DP. Investigating the first-cycle irreversibility of lithium metal oxide cathodes for Li batteries. *Journal of Materials Science* **43**, 4701-4706 (2008).
34. Genovese M, Louli AJ, Weber R, Hames S, Dahn JR. Measuring the Coulombic Efficiency of Lithium Metal Cycling in Anode-Free Lithium Metal Batteries. *Journal of The Electrochemical Society* **165**, A3321-A3325 (2018).

35. Zhou H, Xin F, Pei B, Whittingham MS. What Limits the Capacity of Layered Oxide Cathodes in Lithium Batteries? *ACS Energy Letters* **4**, 1902-1906 (2019).
36. Teshager MA, Lin SD, Hwang B-J, Wang F-M, Hy S, Haregewoin AM. In Situ DRIFTS Analysis of Solid-Electrolyte Interphase Formation on Li-Rich Li1.2Ni0.2Mn0.6O2 and LiCoO2 Cathodes during Oxidative lectrolyte Decomposition. *ChemElectroChem* **3**, 337-345 (2016).
37. Lin M-H*, et al.* Revealing the mitigation of intrinsic structure transformation and oxygen evolution in a layered Li 1.2 Ni 0.2 Mn 0.6 O 2 cathode using restricted charging protocols. *Journal of Power Sources* **359**, 539-548 (2017).
38. Lee H*, et al.* Detrimental Effects of Chemical Crossover from the Lithium Anode to Cathode in Rechargeable Lithium Metal Batteries. *ACS Energy Letters* **3**, 2921-2930 (2018).
39. Fang C*, et al.* Quantifying inactive lithium in lithium metal batteries. *Nature* **572**, 511-515 (2019).
40. Zhang X-Q, Cheng X-B, Chen X, Yan C, Zhang Q. Fluoroethylene Carbonate Additives to Render Uniform Li Deposits in Lithium Metal Batteries. *Advanced Functional Materials* **27**, (2017).

Acknowledgements

Financial support from the Ministry of Science and Technology of Taiwan (108-3116-F-011-001-CC1, 108-2627-M-011-001-, 107-2923-E-011-002, 107-2119-M-002-033-, 106-2923-E 011-005, 106-2221-E-011-125-MY3), the Ministry of Education of Taiwan (U2RSC program, MOE 1080059, Taiwan's Deep Decarbonization Pathways toward a Sustainable Society Project (AS-KPQ-106-DDPP) from Academia Sinica as well as the facilities of support from National Taiwan University of Science and Technology (NTUST) and National Synchrotron Radiation Research Centre (NSRRC) are all gratefully acknowledged.

Author contributions

C.-J. H. and B.J. H. conceived and designed the work; C.-J. H., B. T., H.-C. T., K.N. S., H. S., T. T. H., T.T. B., and L.-M. K. performed the experiments; C.-J. H., B. T., H.-C. T., H. S., T. T. H., T.T. B., L.-M. K., W.-N. S., and B.J. H. analyzed the data; C.-J. H. and B.J. H. wrote the paper. All the authors discussed the results and commented on the manuscript. All authors have approved the final version of the manuscript.

Additional information

Supplementary information including *in-situ* OM movies are available in the online version of the paper.

Correspondence and requests for materials should be addressed to B.-J. H.

Competing interests: The authors declare no competing interests.

Figures

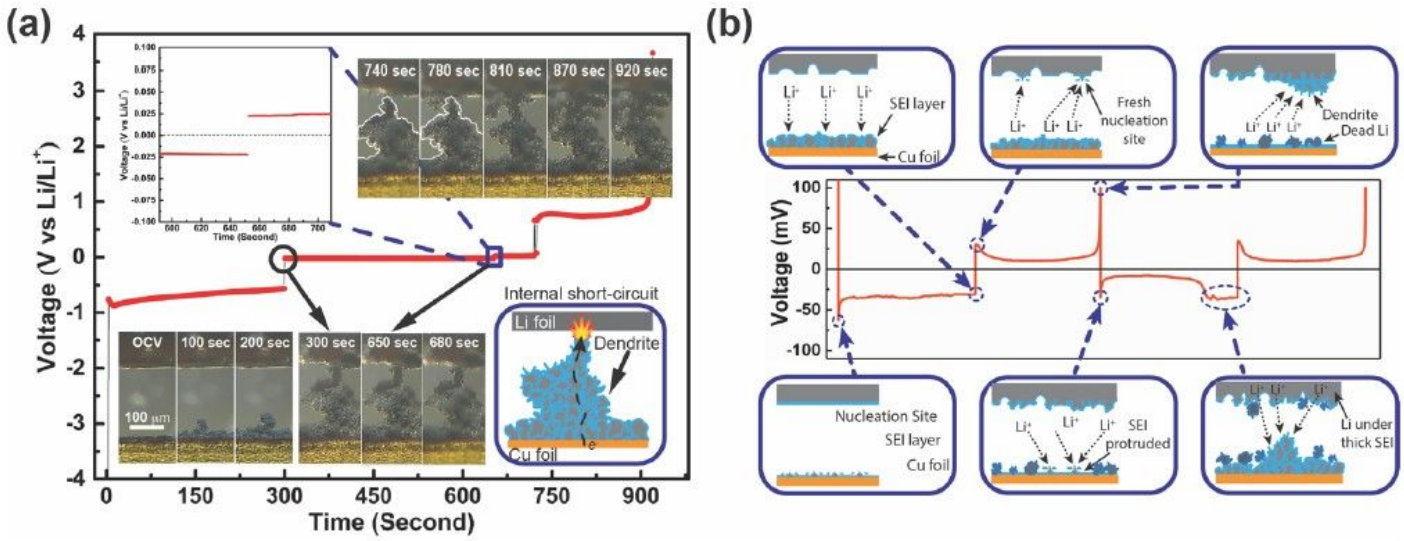

Figure 1

In-situ OM and Li deposition/dissolution scheme. a, In-situ OM measurement of Li deposition/dissolution on Cu electrode under ultra-high current density of 500 mA cm-2 for demonstration of short-circuit. b, Scheme of Li deposition/dissolution on Cu foil during cycling of Li//Cu cell under current density of 0.2 mA cm-2.

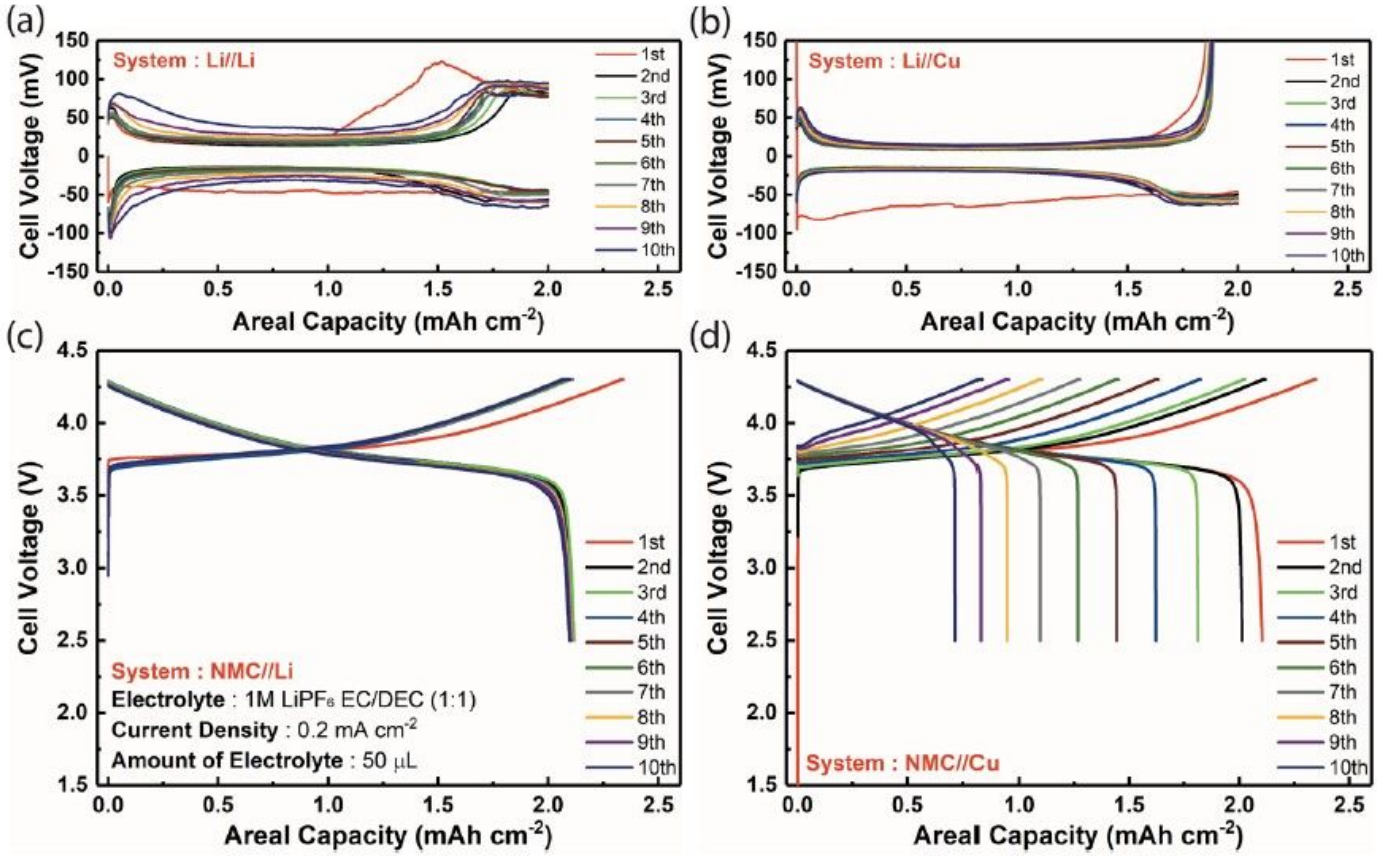

Figure 2

Electrochemical charge and discharge curves. a, Li//Li. b, Li//Cu. c, NMC//Li. d, NMC//Cu. All the cells use 1M LiPF6 in EC/DEC (1:1) as electrolyte with the current density of 0.2 mA cm-2. We selected NMC-111 as the cathode material used in this electrolyte, one can substitute desired cathode material for cathode study in cathode/Li cell and AFLMB.

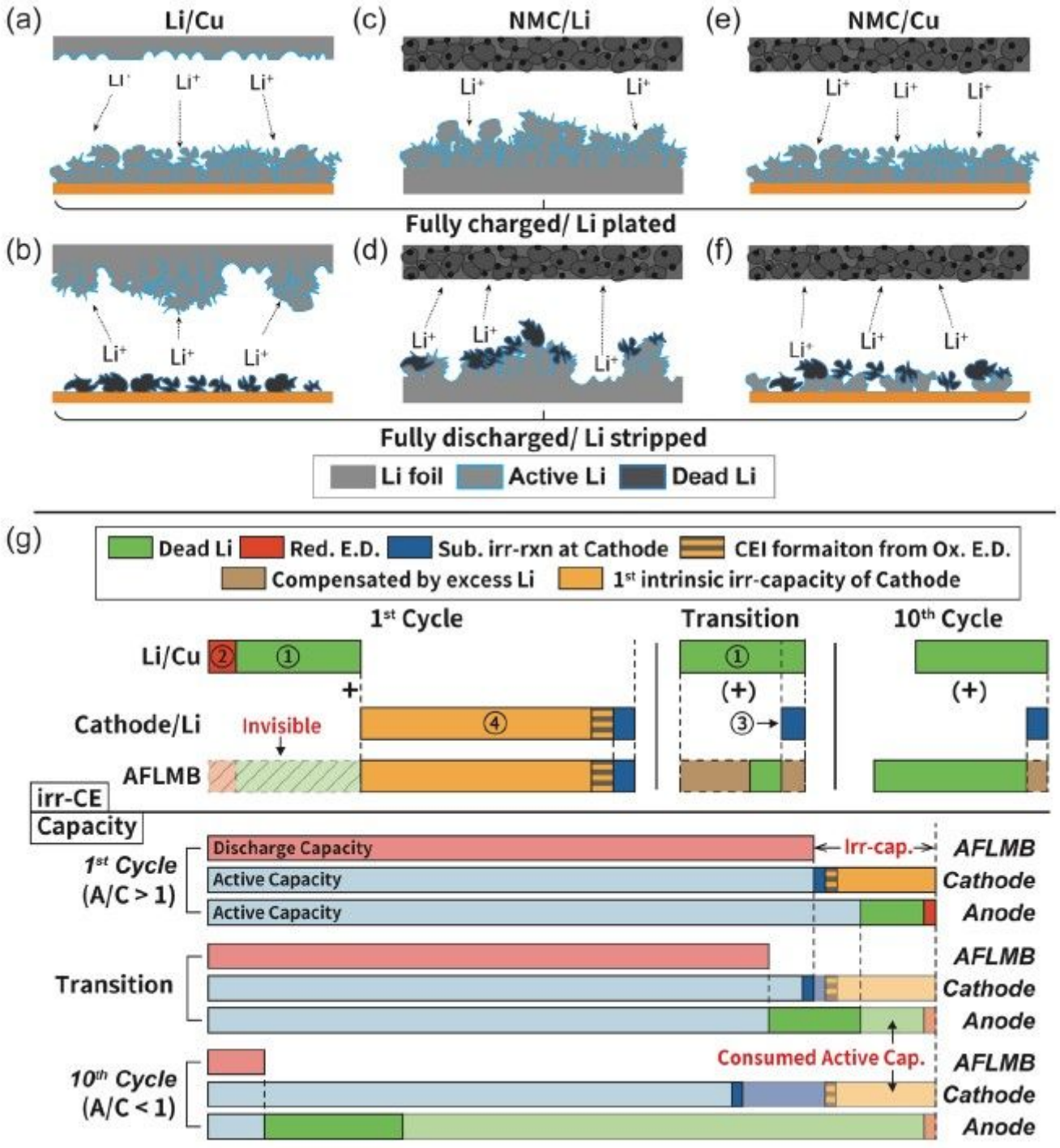

Figure 3

Integrated protocol and scheme of different cell configuration at fully charged and discharged states. a, b, c, Scheme of Li//Cu, NMC//Li, and NMC//Cu cells at fully charged/ Li pated sate in the first cycle, respectively. d, e, f, Scheme of Li//Cu, NMC//Li, and NMC//Cu cells at fully discharge/ Li stripped state in the first cycle, respectively. g, Proposed integrated protocol to unravel the origins of irreversible CE in AFLMB by Li//Cu and cathode/Li cells. The blue shell on Li represents the SEI layer. Red. E.D. stands for the reductive electrolyte decomposition, Ox. E.D. for oxidative electrolyte decomposition, and sub. irr-rxn for subsequent irreversible reactions, respectively.

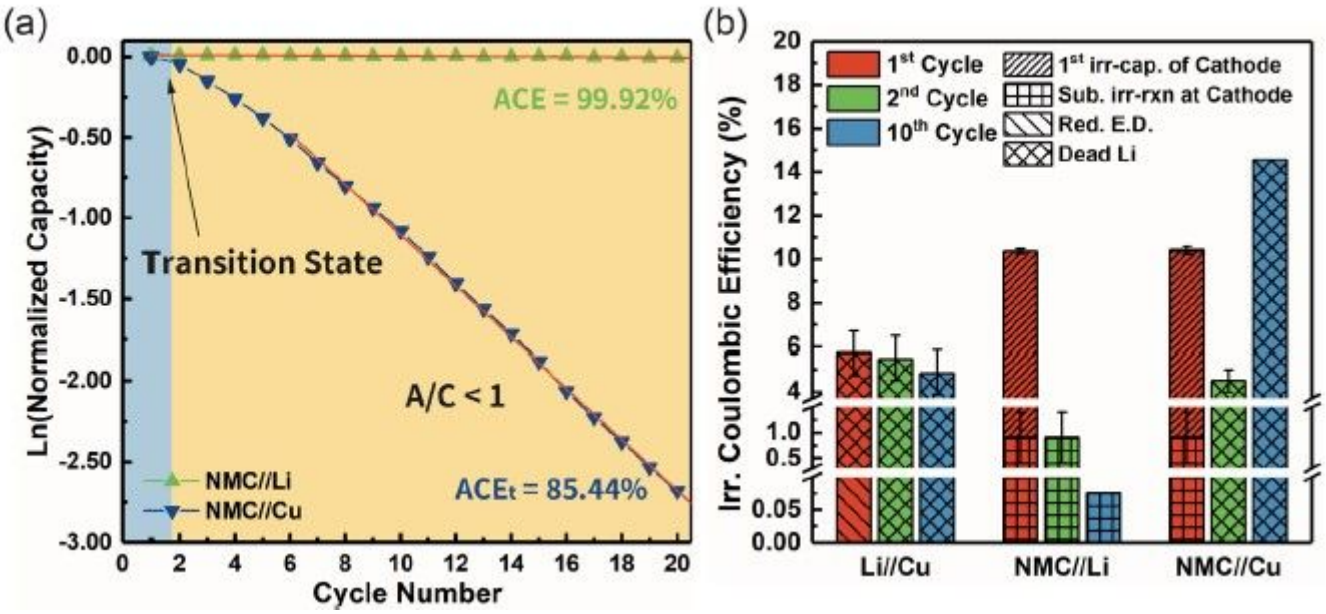

Figure 4

Results obtained from integrated protocol using 1M LiPF6 in EC/DEC (1:1) as electrolyte under 0.2 mA cm-2. a, Normalized discharge capacity versus cycle number of NMC//Li and NMC//Cu cells. b, irreversible CE comparison of four cell set-ups using 1M LiPF6 in EC/DEC (1:1) as electrolyte with the current density of 0.2 mA cm-2. NMC-111 electrode with an areal capacity of ~2 mAh cm-2 was used as the cathode electrode for demonstration in this work. The 10th cycle irr-CE of NMC//Li and NMC//Cu cells shown here and for the rest of the examples in this work are the average irr-CE extracted from the linear fitted results of ln(normalized capacity) versus cycle number to present a more general and reliable irr-CE. It should be noted the average irr-CE of NMC//Cu cell is calculated after transition state, namely in the region of A/C ratio < 1. The capacity retention comparison of NMC//Li and NMC//Cu cells are shown in Fig. S5a.

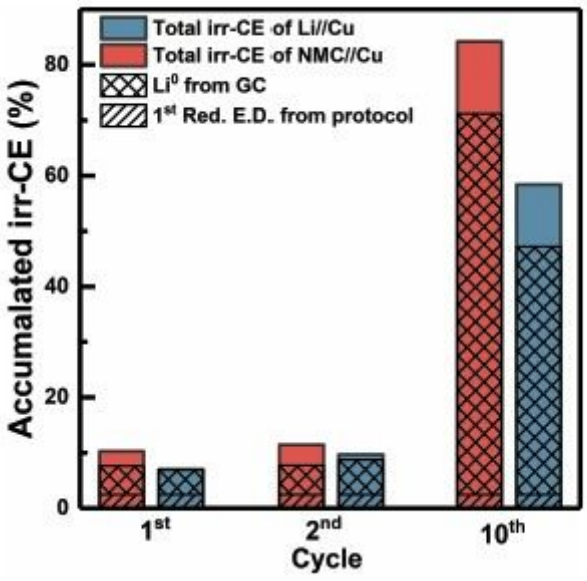

Figure 5

Dead-Li validation for the irr-CE obtained from the proposed protocol using the titration gas chromatography method.

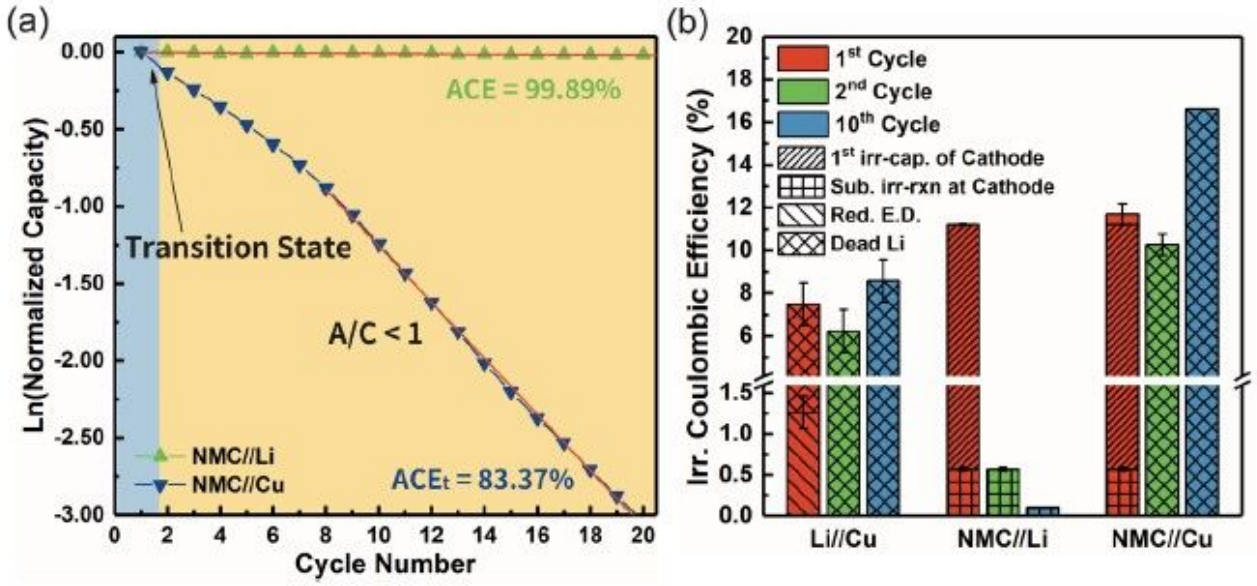

Figure 6

Results obtained from integrated protocol using 1M LiPF6 in EC/DEC (1:1) as electrolyte under 0.4 mA cm-2. a, Normalized discharge capacity versus cycle number of NMC//Li and NMC//Cu cells. b, irreversible efficiency comparison of four cell set-ups using 1M LiPF6 in EC:DEC as electrolyte with the current density of 0.4 mA cm-2. The capacity retention comparison of NMC//Li and NMC//Cu cells are shown in Fig. S5b. The charge/discharge profiles of each cell configuration are shown in Fig. S9.

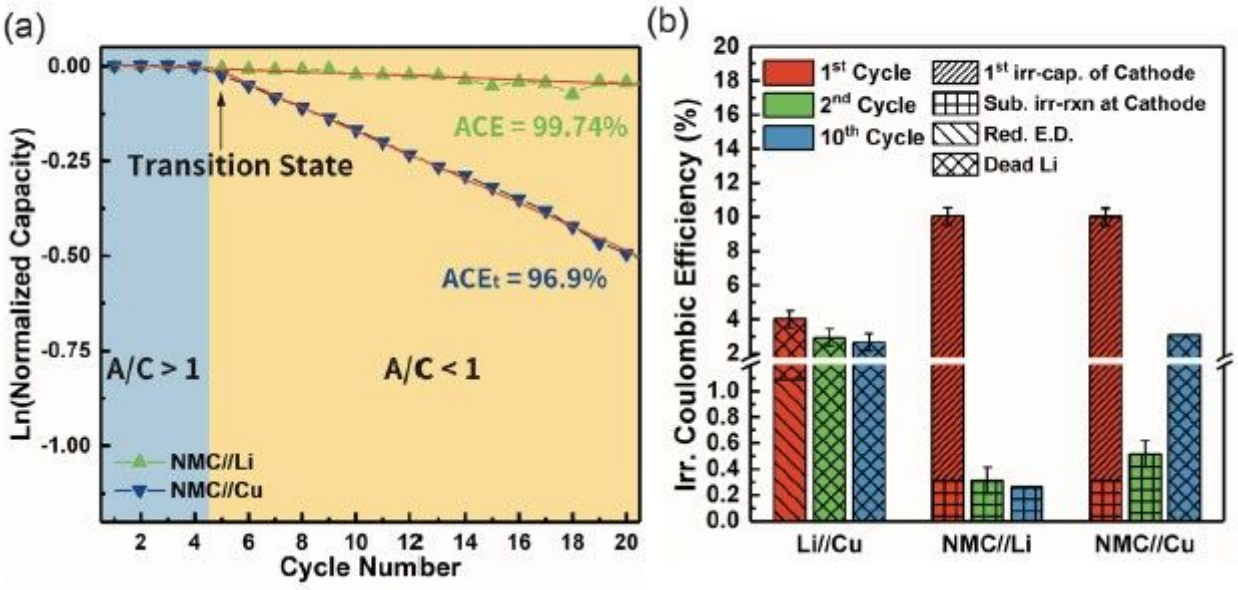

Figure 7

Results obtained from integrated protocol using 1M LiPF6 in EC/DEC (1:1) with 5% FEC added as electrolyte. a, Normalized discharge capacity versus cycle number of NMC//Li and NMC//Cu cells. b, irreversible CE comparison of four cell set-ups using 1M LiPF6 in EC/DEC (1:1) with 5% FEC added as electrolyte with the current density of 0.2 mA cm-2. The capacity retention comparison of NMC//Li and NMC//Cu cells are shown in Fig. S5c. The charge/discharge profiles of each cell configuration are shown in Fig. S10.

Supplementary Files

This is a list of supplementary files associated with this preprint. Click to download.

- ProtocolNatcommSI0717.pdf
- 2672500supp4775738qdnpfw.pdf
- plattingVideo.mp4
- strippingVideo.mp4
- shortCircuit.mp4